LA-UR-13-27585

Author(s):   Grim, Gary P.
              Morgan, George L.
              Aragonez, Robert J.
              Archuleta, Thomas N.
              Bower, Dan
              Danly, Christopher R.
              Drury, Owen B
              Dzenitis, John M.
              Fatherley, Valerie E.
              Felker, Brian
              Fittinghoff, David .
              Guler, Nevzat
              Merrill, Frank E.
              Oertel, John A.
              Wilde, Carl H.
              Wilke, Mark D.

Los Alamos
NATIONAL LABORATORY
———— EST.1943 ————

The 27.3 meter neutron time-of-flight system for the National Ignition Facility

G. P. Grim,[a] G. L. Morgan,[a] R. Aragonez,[a] T. N. Archuleta,[a] D. E. Bower,[b] C. R. Danly,[a], O. B. Drury[b], J. M. Dzenitis,[b] V. E. Fatherley,[a] B. Felker,[b] D. N. Fittinghoff,[b] N. Guler,[a] F. E. Merrill,[a], J. A. Oertel,[a], C H Wilde,[a] and M. D. Wilke[a,c]

[a]Los Alamos National Laboratory, PO Box 1663, Los Alamos, NM 87545, USA
[b]Lawrence Livermore National Laboratory, 7000 East Rd., Livermore, CA 94551, USA
[c] Deceased

ABSTRACT

One of the scientific goals of the National Ignition Facility (NIF) at Lawrence Livermore National Laboratory, Livermore CA, is to obtain thermonuclear ignition by compressing 2.2 mm diameter capsules filed with deuterium and tritium to densities approaching 1000 g/cm^3 and temperatures in excess of 4 keV. The fusion reaction $d + t \rightarrow n + \alpha$ results in a 14.03 MeV neutron providing a source of diagnostic particles to characterize the implosion. The spectrum of neutrons emanating from the assembly may be used to infer the fusion yield, plasma ion temperature, and fuel areal density, all key diagnostic quantities of implosion quality. The neutron time-of-flight (nToF) system co-located along the Neutron Imaging System line-of-site, (NIToF), is a set of 4 scintillation detectors located approximately 27.3 m from the implosion source. Neutron spectral information is inferred using arrival time at the detector. The NIToF system is described below, including the hardware elements, calibration data, analysis methods, and an example of its basic performance characteristics.

Keywords: Neutron time-of-flight, Inertial Confinement Fusion, Scintillators

1. INTRODUCTION

Neutron time-of-flight techniques have been used from the earliest days of High Energy Density physics facilities.[1–3] Neutrons are generally produced in these facilities through nuclear reactions in a hot plasma of hydrogen fuel. For example, the reaction $d + t \rightarrow n + \alpha$ produces 14.03 MeV neutrons in the rest frame of the fusing ion pair. Since the plasma is hot, $\sim$ 3-10 KeV, and the surrounding mass can be thick, $\sim$ 1 g/cm^2, the kinetic energies of the neutrons exiting the plasma will be a spectrum.[4–6] Further, since the time interval over which neutrons are produced and transit the plasma are very short, O(100) ps, it is possible to measure an emitted neutron's velocity by measuring its time-of-flight over a sufficiently long distance, usually a few meters. With this spectral knowledge it is possible to infer properties of the plasma, such as ion temperature,[5,7] or areal density,[3,8] which is a powerful microscope into the performance of the implosion process.

There are a number of neutron time-of-flight[9,10] detector systems at the National Ignition Facility, Lawrence Livermore National Laboratory, Livermore CA, using a variety of different detector technologies, from organic scintillators with photo-detector readout, to single crystal diamond ionization chambers. Here we report on one such detector system, the Neutron Imaging Time-of-Flight (NIToF) system. The NIToF system is a set of four detectors, co-located with the Neutron Imaging System (NIS) diagnostic. The four detectors include two in-beam detectors for measuring neutron time-of-flight over a large range of neutron yields, as well as two out-of-beam, background detectors to quantify the contribution of scattered radiation to the in-beam signal. The NIToF system has the longest flight path at the NIF, just over 27 m, and the narrowest instrument response function, giving it the most sensitive spectral measurement capability. In the following sections a description of the NIToF system is presented including the hardware, relevant calibration and performance data, as well as a sample ion temperature analysis.

Send correspondence to: E-mail: gpgrim@lanl.gov, Telephone: 1 (925) 423-1058
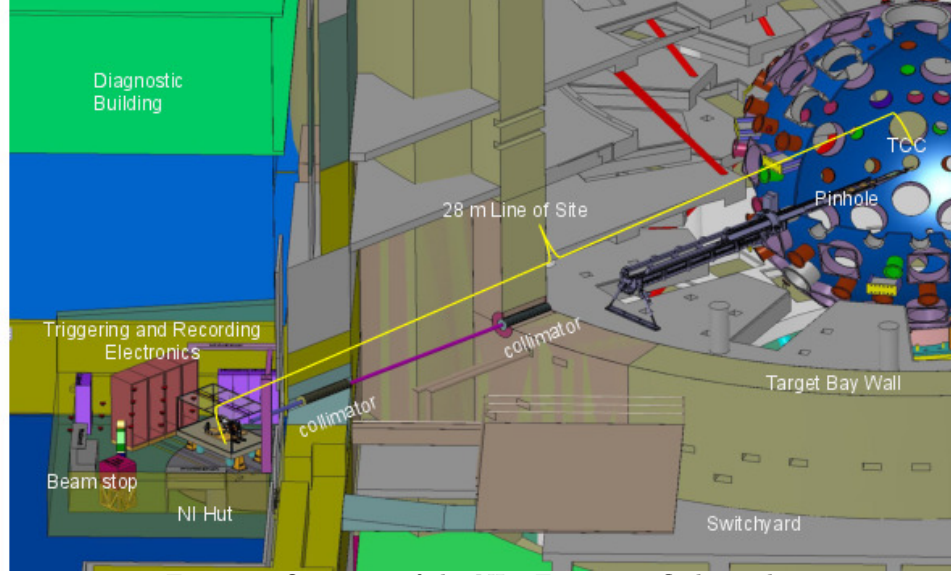
Figure 1: Overview of the NIToF neutron flight path.

2. NITOF HARDWARE

The NIF NIToF system is a fast neutron, time-of-flight detection system comprised of long (~ 27.3 m) collimated flight-path, with two thin, in-beam plastic scintillation paddles, readout by fast photo-detectors, and 2 out of beam detectors, used to characterize the "room-return" background radiation generated by the mass of the nearby neutron imaging system. Details on the major components of this system are presented in the following sections.

2.1 NIToF Flight Path

Fig. 1 shows the flight path for neutrons detected in the NIToF system. Fast neutrons born at the center of the 10 m diameter NIF target chamber pass through the very fine collimation of the neutron imaging aperture and exit the aperture through a 3 mm glass mirror. After the aperture, the neutrons traverse another 9.5 m of vacuum, where they exit through a 1 cm thick Al window into air, where they travel the remaining 17 m to the NIToF system. Along the 17 m of air, the neutrons pass through a 3 mm thick Al window just before the first of two beam path defining collimators.

Fig. 2a shows a close up of the exiting end of the neutron imaging system aperture. This fine collimation assembly is a compound system with three penumbral and 20 pinhole apertures formed in a 20 cm long sandwich of Au foils and W blocks.[11, 12] Approximately 91% of the neutrons detected in the NIToF system pass through the thee penumbral apertures. These apertures have a biconic profile, with a limiting diameter of 300 μm at the center of the assembly. The front face of the aperture is located 32.5 cm from the neutron source and the aperture views a 200 μm diameter area around this point. This narrow field-of-view ensures that neutrons passing through the aperture are from the imploded capsule, and not from scatters in the mass near the center of the target chamber. The aperture body cross sectional area casts an 80×80 cm^2 shadow at the NIToF detectors.

As mentioned, the beam path in air includes several collimation assemblies located at 15.4 m, 17.1 m, 23.4 m, and 25.6 m from target chamber center (TCC) before passing into the neutron imaging annex where the detectors reside. The collimation assemblies at each position are made using a set of 1.5 in. thick, 304 stainless steel annuli, with inner diameters given in Fig. 2b. The beam line defined by the collimators overfills both the NIToF and neutron imaging detectors, though the fine collimation of the neutron imaging aperture, underfills these detectors.

To perform neutron spectral measurement the neutron flux must be corrected for attenuation due to material along the flight path. Fig. 3 shows the calculated transmission at the NIToF detector position using the neutron
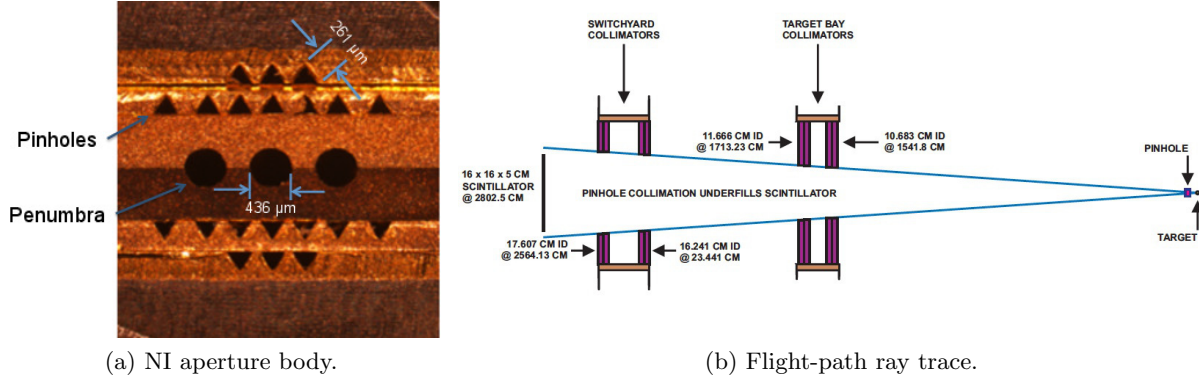
(a) NI aperture body.
(b) Flight-path ray trace.

Figure 2: Panel 2a shows the exiting face of the neutron imaging system aperture. The majority of the neutrons detected in the NIToF system pass through the penumbral apertures, which have a biconic shape with a 300 μm diameter at the center of the aperture body, 42.5 cm from target chamber center. Panel 2b shows a ray trace of the collimators and aperture defining the NIToF/NIS flight path.
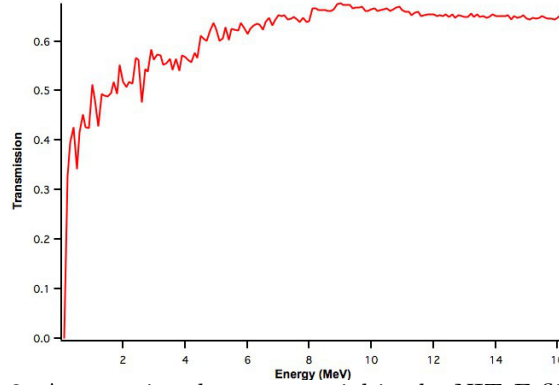

Figure 3: Attenuation due to material in the NIToF flight path.

transport code MCNP.[13] At 14 MeV approximately 61% of the neutrons leaving the imploded capsule arrive at the NIToF system. This drops to $\sim 50\%$ for 2 MeV neutrons. This relative correction is important when measuring the spectrum of neutrons produced by the reaction $t + t \rightarrow 2n + \alpha$.

2.2 The NI Annex

Fig. 4 shows the neutron imaging and NIToF detector systems in the neutron imaging annex. Neutrons exit the collimators and pass through the NIToF scintillator paddles, located 27.27 m and 27.35 m from target chamber center, and then into the neutron imaging system, located 28 m from TCC. To ensure good quantum efficiency the NIS scintillator and optical relay system are thick, scattering roughly 99% of the beam passing through these elements, and generating significant backgrounds within the room. To measure the level of these backgrounds, two out-of-beam background detectors are located on the table, as indicated, and approximately 70 cm from the neutron imaging system.

2.2.1 Scintillator Paddles

Fig. 5 shows the design of the NIToF scintillator paddles. The paddles were made by Eljen Technologies, using their EJ-200 scintillator, which is chemically the same as the materials bearing the historical names Pilot F, NE-111, and BC-408. This material was chosen based on the properties published by the manufacturer, including its relative brightness at 64% of anthracene, good efficiency with $\sim 10{,}000$ photons per MeV electron-equivalent, and fast response, rise and fall times of 900 ps rise and 2.1 ns respectively. The material is made using a PVT base, with a density of 1.023 g/cm^3 and refractive index of 1.58. The spectral response peaks in the blue, at 425 nm, making it a good choice for general purpose photo-detectors using S20 photocathodes. The active volume
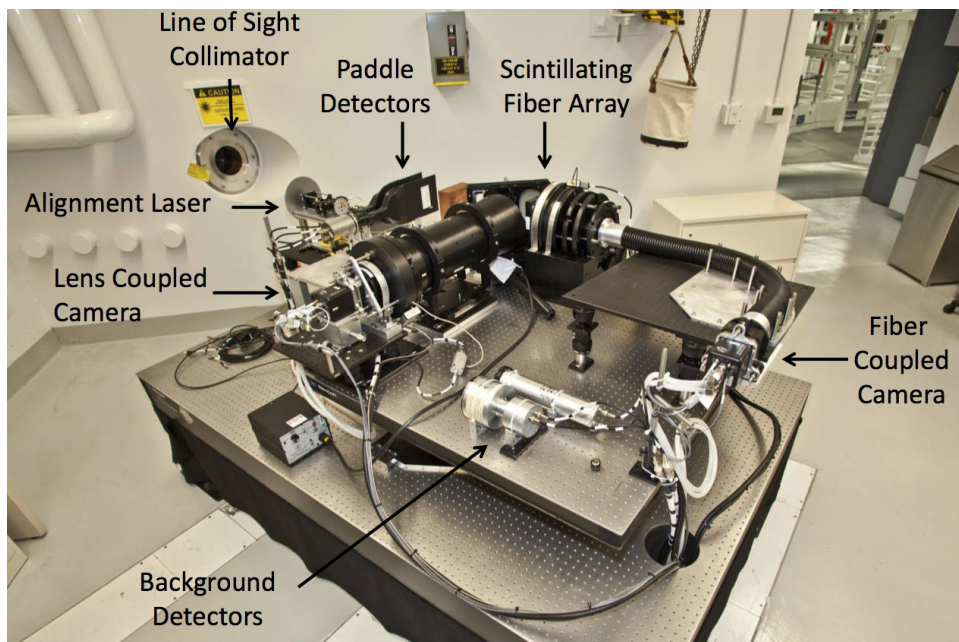
Figure 4: The NIF neutron imaging system detector table. Neutrons enter from the upper left, passing slightly downward and to the right. The NIToF in-beam paddle detectors are shown in the upper left, and the background detectors are visible in the middle of the picture.
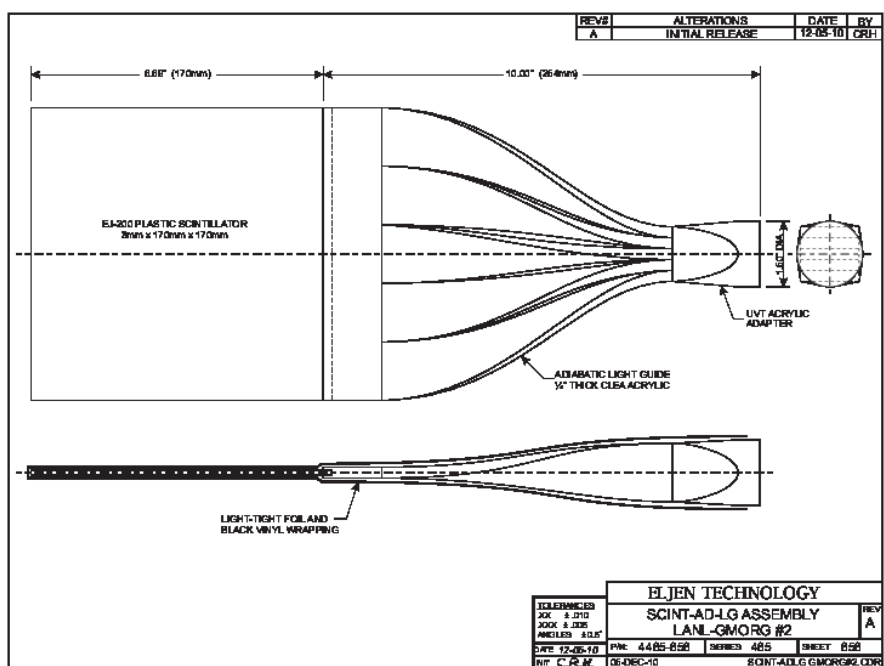
Figure 5: Drawing of the NIToF in-beam scintillation paddle. To avoid generating non-uniform shadowing, or excess scattering in front of the neutron imagine system, the paddle is constructed from a $17 \times 17 \times 0.3$ cm^3 piece of EJ-200 (NE-111A/BC-408 equivalent) scintillator from Eljen Technologies. The light from the paddle is relayed to a UVT plug through an adiabatic light guide constructed from acrylic.

| Component	τ (ns)	Relative Strength (%)
1	1.84	1
2	8.6	3.0
3	82.5	0.23

Table 1: Decay components extracted from Fig. 6a by assuming the sum of three exponential decay functions convolved with a gaussian detector response.

of the paddles is $17 \times 17 \times 0.3$ cm^3, with the large area cross section designed to uniformly shadow the 16×16 cm^2 neutron imaging scintillator. The 3 mm thickness was chosen to optimize the detected signal without creating a significant scattering source for the imager. One edge of the scintillator is butt coupled to a set of clear acrylic light guides, which adiabatically relay the scintillation light to an acrylic adapter for coupling to a photo-detector. The assembly is then covered in light-tight foil and black vinyl wrapping. The optical through delay from the center of the scintillator to the end of the optical plug is ~ 925 ps.

2.2.2 Scintillator Characteristics

To facilitate accurate physics measurements, the response function of the in-beam detectors must be well characterized. Below we present measurements and calculations of several key properties of the scintillator, including measurements of the decay curve, as well as neutron and gamma sensitivity as a function of energy.

Fig. 6a shows the temporal response of EJ-200/NE-111 scintillator to individual neutrons from the spectrum produced by an AmBe source. These measurements used the time-correlated single photon counting technique[14] augmented with a time-of-flight capability to discriminate between photons and neutrons emanating from the source. The measurements were taking using a 2×2 cm cylindrical sample. It is assumed that light emission from the scintillator in response to an impulse of radiation is the sum of three exponential decay functions with different lifetimes, i.e:

$$L(t) = \frac{A_1}{\tau_1} exp\left(t/\tau_1\right) + \frac{A_2}{\tau_2} exp\left(t/\tau_2\right) + \frac{A_3}{\tau_3} exp\left(t/\tau_3\right) \tag{1}$$

To extract the, A$_{1-3}$, and τ_{1-3}, the data shown in Fig. 6a were fit to the function $L(t)$ convolved with a gaussian function, to account for the impulse response of the photo-detector system. The resulting fit data are shown in Tab. 1.

The fast decay constant, $\tau_1 = 1.84$ ns, is typical of unquenched fast plastic scintillators and is in reasonable agreement with the manufacturers published value. To the best of our knowledge this is the first time that the values for the second and third decay constants have been published. The fast first component, and relative weakness of the 2nd and 3rd components, ensure that temporal measurements of slower neutrons will not be significantly impacted by residual light in the scintillator.

In addition to the impulse response of the scintillator, the relative sensitivity of the material to both gammas and neutrons is required to properly interpret spectral information and subtract background contributions. Fig. 6 shows a calculation of the scintillator sensitivity, in units of MeV-electron equivalence, for both neutrons and gammas. The neutron sensitivity was calculated using the SCINFUL[15] code produced by Oak Ridge National Laboratory. The SCINFUL code is designed to calculate the scintillator response to neutrons from 0.1 to 80 MeV, including light production from both elastic and non-elastic processes in the scintillator material, *e.g.* H(n,p), C(n,α), and C(n,3α) etc. Absolute sensitivities were determined using a source range calibration provided by National Security Technologies, Las Vegas Operations. Gamma sensitivity was calculated using the EGS4[16] code, produced by the Stanford Linear Accelerator Laboratory.

(a) Scintillator decay data   (b) Neutron sensitivity   (c) Gamma sensitivity
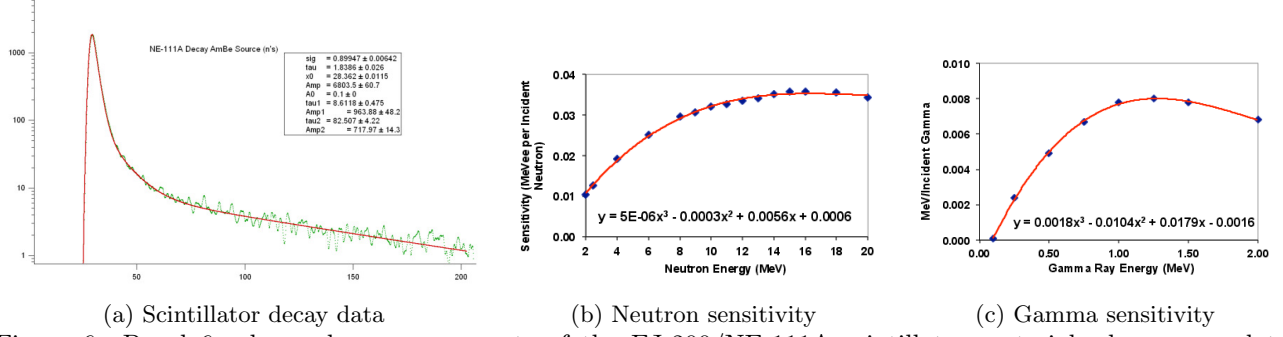
Figure 6: Panel 6a shows decay components of the EJ-200/NE-111A scintillator material when exposed to neutrons from an AmBe source. Three independent decays are observed, a fast 1.84 ns component, followed by two slower components at 8.6 ns, and 82.5 ns. The strengths of the two slow components relative to the fast component are 3.01% and 0.23% respectively. Panels 6b and 6c show the calculations of the NE111A scintillator sensitivity to neutrons and gammas.

2.3 In-Beam Photo-Detectors

To provide a measure of redundancy, as well as dynamic range for measuring the neutron flux, two identical in-beam scintillator paddles are employed, one at 27.27 m from TCC and one at 27.35 m, referred to here as NIToF 27.27 and NIToF 27.35. To provide good dynamic range, with high bandwidth, the respective photo-detectors chosen to readout the two in-beam paddles are a Hamamatsu R5916U-50, and a Hamamatsu R1193U-53.

The R1193U-53 is a large area, multi-alkali, bi-planar photodiode with an intrinsic gain of 1. For high neutron yield experiments, where $Y_n \geq 2 \times 10^{15}$ neutrons, the NIToF 27.35 paddle is the primary detector for analysis. This detector uses a Na-K-Sb-C photocathode with a mesh anode, providing a fast response, 270 ps rise time and 100 ps fall time. The R1193U-53 photocathode response peaks at 400 nm, and is relatively flat in the range of 400 – 500 nm, so it is well matched to the spectral content produced by the EJ-200/NE-111A scintillator.

The R5916U-50 is made with a 10 mm, multi-alkali photo-cathode, with a 2-stage, 6 μm pore, micro-channel plate gain element, providing high-dynamic range with fast response. The peak of the photocathode sensitivity is 430 nm which is also well matched to the scintillator. The detector is linear over a large range of gain values from 10^2 to 10^5, and is quite fast, with rise and fall times of 180 ps and 700 ps respectively, and an impulse response full-width half-maximum of 95 ps. The capacitance between the photo-cathode and micro channel plate is 14.7 pF, providing $\sim$ 9 nC of stored charge for a typical experiment. At neutron yields below 10^{15}, NIToF 27.27 is the primary analysis detector.

Because of the paucity of shots with yields greater than 2×10^{15}, we limit further discussion of the in-beam elements of the NIToF system to the NIToF 27.27 m detector.

To enable physics analysis, the impulse response function (IRF) of the NIToF 27.27 m detector must be unfolded from the data prior to physics analysis. Since it is assumed that the temporal response of the photo-detector is a fast gaussian, the IRF of the NIToF 27.27 m system will be given by a gaussian function convolved with the sum of three exponential decay functions, *c.f.* Eq. 1. The functional form of the IRF may be written as:[7]

$$\sum_{i=1}^{3} A_i \cdot \frac{exp\left(-(t/\tau_i)\,exp\left(\sigma^2/2\tau_i^2\right)\right)}{2\tau_i} \times \left[1 + erf\left(\frac{t - \sigma^2/2\tau_1^2}{\sqrt{2\sigma^2}}\right)\right], \tag{2}$$

where σ represents the gaussian photo-detector response, and the A_i and τ_i, are the components of the scintillator paddle decay. The photo-detector FWHM is comparable in scale to the fast decay component of the scintillator, so some correlation between these parameters can exist during a fit, or unfold. Therefore, the strategy to characterize the parameters of the IRF, was to measure the fast component of the detector IRF using an X-ray

Component	τ (ns)	Relative Amplitude A_i/A_1
σ	0.92	–
1	2.67	1
2	8.6	0.141
3	82.5	0.105

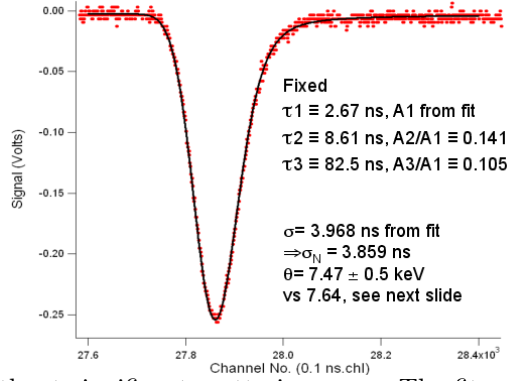Table 2: Parameters of the NIToF 27.27 m impulse response function based on Eq. 2.

Figure 7: Fit to an implosion without significant scattering mass. The fit uses the IRF function, allowing only two parameters to vary, the overall amplitude, and the Gaussian width.

impulse source, and then use the scintillator decay data above *cf.* Tab. 1, for the 2nd and 3rd components. With this strategy, the parameters of the NIToF 27.27 IRF are given in Tab. 2.

It is worth noting that the first component decay time has grown from 1.84 ns to 2.67 ns. This is not unexpected due to the geometry change between the scintillator decay measurement (a 2×2 cm cylinder) and the NIToF paddle (a $17 \times 17 \times 0.3$ cm^3 parallelepiped) IRF measurement. A qualitative test of the veracity of this approach is shown in Fig. 7. The dots in the figure are the 100 ps spaced sampled points from the NIToF 27.27 m detector, where 14.1 MeV neutrons were produced in a very low mass implosion. The lack of scattering in the plasma that produced the neutrons preserves the nearly gaussian shape of the doppler broadened spectrum due to the thermal plasma. The trace overlaying the data, is the fit to the data using the functional form of the IRF, but two free parameters, an overall constant multiplier on the IRF to address the neutron yield, and the gaussian σ, to account for the contribution to the signal from thermal broadening. These data indicate that the IRF used performs well at describing the response of the system.
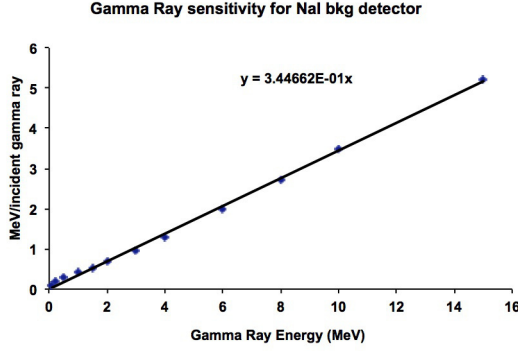
2.4 Background Detectors

Because of the large scattering mass of neutron imaging system, located ~ 70 cm downstream of the NIToF detectors, background measurements of the scattered radiation in the room are important for correcting the NIToF data. We have employed two separate out of beam detectors on the neutron imaging detector table, to directly measure these backgrounds.

The gamma background detector is comprised of a 2×2 cm cylinder of NaI material coupled to an XP2242 photo-detector. This detector provides excellent sensitivity to gammas. Although the NaI scintillator decay is relatively slow at 250 ns, the data are unfolded using the known response, providing good estimate of the temporally resolved flux of gammas produced in the scattering mass. The neutron background detector is a 5×3.25 in. cylindrical sample of BC-422 plastic scintillator readout by a Hamamatsu R5946 phototube. The R5946 has a 27 mm, bi-alkali photo-cathode with a 16 stage mesh dynode structure, providing linear gain over a large dynamic range.

The two background detectors are located the same distance from the neutron imaging system scattering mass as the in-beam paddle detectors, therefore subtraction of the background signals does not require a temporal shift. Since the detector geometries are different, their sensitivities are also calculated, as shown in Fig. 8,
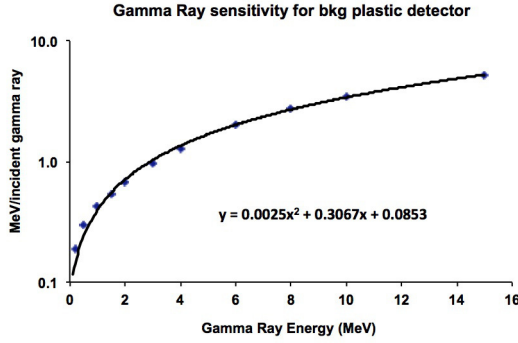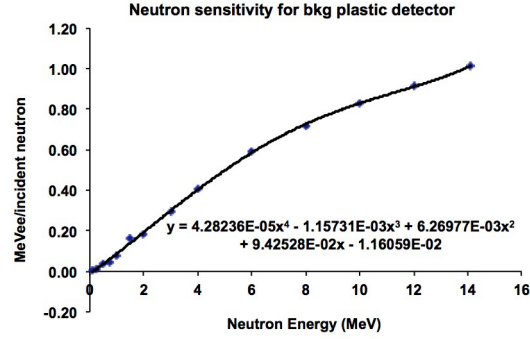
(a) NaI gamma sensitivity
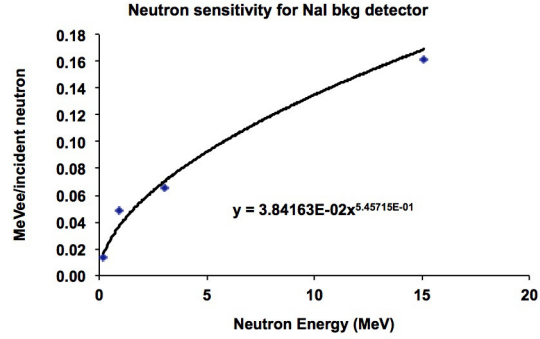
(b) NaI neutron sensitivity

(c) Plastic gamma sensitivity

(d) Plastic neutron sensitivity

Figure 8: Calculation of the gamma and neutron scintillator sensitivities for the two background detectors in the NIToF system.

and the relative sensitivity of the neutron and gamma signals to the in-beam detectors is used to correct the background data for subtraction from the in-beam signals. The sensitivities presented in Fig. 8 were calculated using the same approach as the in-beam paddles. The neutron sensitivity of the NaI detector was calculated based on the work of Thompson.[17]

3. IRF UNFOLDING

There are two primary uses of the data provided by the NIToF detector, determination of the plasma ion-temperature and areal density. Since the data are recorded in the time domain and the arrival time is used to determine neutron velocity, it is essential to remove the temporal response of the detector, through an unfolding process, prior to converting the data to the energy domain for subsequent analysis. The unfolding algorithm used for the NIToF data, called FERD, was developed in the 1960's to enable fast neutron spectroscopy experiments,[18] where the energy dependent pulse height distribution distorts the underlying spectrum passing through the detector. In the NIToF application, the temporal response of the scintillator detector system is distorting the underlying arrival time distribution passing through the detector. Therefore in the NIToF application, the energy domain of the algorithm is exchanged for the time domain, and the energy dependent pulse height response is replaced by the non-gaussian temporal response. Unlike most inversion or deconvolution algorithms, where the goal is to model the underlying distribution by inverting the data with the response function, the strategy of the FERD algorithm is to model the signal produced by an idealized gaussian detector, given the observed data and known non-gaussian response functions. Given this strategy, it is necessary to choose the width of the gaussian response function to be large enough to reduce noise in the system by averaging over time bins, but narrow
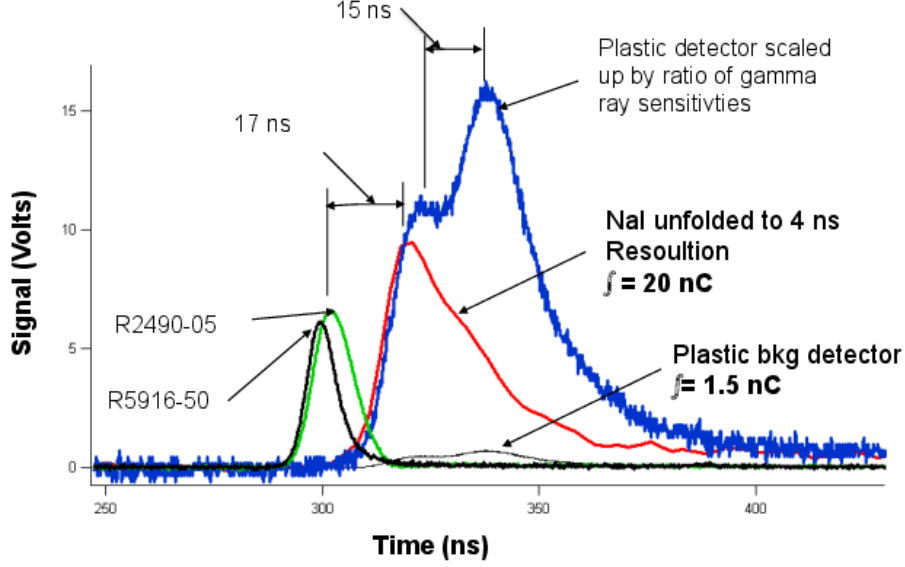
Figure 9: Example of data from the various detectors in the NIToF system. The black and green traces are the in-beam NIToF detectors, where the R1193 PMT at 27.35 m was replaced with an R2490 PMT. The red trace is the background gamma signal, and the blue trace background neutron signal, scaled by the relative gamma sensitivities of the two background detectors.

enough to maintain fidelity with the intended physics analysis. For the data presented below, a 3 ns FWHM gaussian response is used for the in-beam detectors, and a 4 ns FWHM gaussian response is used for the NaI background detector.

3.1 Example Data

An example of the full NIToF data set is given in Fig. 9. In this data set the R1193 detector had not been implemented yet, instead an R2490-05 tube was used. The near coincident black and green traces, labeled R5916-60 and R2490-05, represent the time shifted neutron time-of-flight signals observed in the NIToF 27.27 m detector and the NIToF 27.35 m detectors. The detector responses have not be unfolded from these data. The red trace is the unfolded (4 ns FWHM) signal recorded by the NaI background detector. The leading edge of the gamma signal occurs approximately 17 ns after the neutrons pass through the in-beam paddles. This time difference is consistent with the flight time of 14 MeV neutrons from the paddle to the imaging mass ($\sim$ 15 ns), and for photons to travel from the imaging mass too the NaI detector ($\sim$ 2.3 ns). The thin black trace near the baseline of the plot is the signal produced by the neutron background detector. The blue trace is scaled version of the neutron background signal, using the ratio of the gamma sensitivities of the two background detectors. The comparable height of the leading edge of the red and blue traces shows good agreement on the strength of the gamma signal near the background detectors. The second rising edge that occurs approximately 15 ns later, shows the arrival of slower scattered neutrons at the plastic background detector. The amount of integrated charge observed in the two detectors is indicated on the plot with the NaI detector accumulating 20 nC, and the plastic detector accumulating 1.5 nC. Detailed Monte Carlo calculation of the backgrounds generated by the neutron imaging system mass, folded with the known detector sensitivities agree very quell with these numbers

3.2 Ion Temperature

Fig. 10 shows an example analysis of plasma ion temperature. The data are from a layered cryogenic implosion at the NIF,[19–21] shot number N130812. Under the assumption of a single temperature plasma, where only thermal motion contributes to the neuron spectrum, the relationship between the FWHM, Δ_n, of the 14.1 MeV neutron arrival time at a distance L from the target, and the ion temperature of the plasma, θ is given by:[5]

$$\theta_{DT} = \left(\frac{\Delta_n}{0.122 \cdot L} \right)^2 . \tag{3}$$
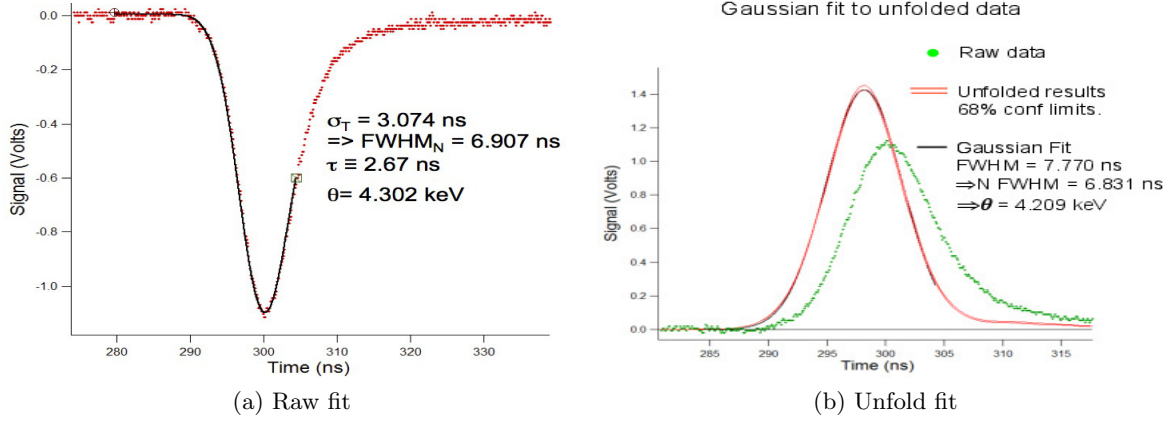
(a) Raw fit (b) Unfold fit

Figure 10: Illustration of the two different methods of calculation ion temperature using the NIToF 27.27 m detector. See text for details.

Fig. 10a shows the raw data (red dots) from the NIToF 27.27 detector, zoomed into the region around the arrival of the thermally broadened 14.1 MeV peak. Overlaid on the data is a fit (black line), using the first component of Eq. 2 plus a linear background function, *i.e.* the fit parameters include A_1, σ, and the linear background terms. Only the first scintillator decay component was used since the fit only covers a few nanoseconds beyond the peak. The resulting σ from the fit gives: $\sigma_{fit} = 3.704$ ns, and includes contributions from the IRF, ($\sigma_{det} = 0.92$ ns), and the spread in the neutron arrival time due to thermal broadening, σ_n. Since these are assumed to be gaussian distributions, σ_n is then given by $\sqrt{\sigma_{fit}^2 - \sigma_{det}^2}$, resulting in $\Delta_n = 6.91$ ns, and an ion temperature of $\theta = 4.3$ keV.

The uncertainty in the measurement is given by:

$$\left(\frac{\delta\theta_{DT}}{\theta_{DT}}\right)^2 = \left(\frac{\delta L}{L}\right)^2 + \left(\frac{\delta\sigma_{fit}}{\sigma_{fit}}\right)^2 + \left(\frac{\delta\sigma_{det}}{\sigma_{det}}\right)^2 \tag{4}$$

$$\approx 2\left(\frac{\delta\sigma_{fit}}{\sigma_{fit}}\right)^2, \tag{5}$$

as $\delta L/L \approx 0$, and the fit and detector σ uncertainties are comparable. A typical range of $\delta\sigma/\sigma$ is $1\% - 2\%$, which results in $\delta\theta/\theta \sim 3\% - 6\%$. For a typical ignition experiment with $\theta \sim 3$ keV, this corresponds to an uncertainty range of 90 to 170 eV.

Fig. 10b shows an alternative method for determining the plasma ion temperature. In this case, the data are unfolded using the methodology described in Sec. 3. The green trace in the figure shows the inverted and baseline shifted raw data, while the red traces provide the 68% confidence interval after unfold. The resulting fit to the mean of the confidence interval gives a $\sigma_{fit} = 7.70$ ns. The neutron arrival FWHM is then calculated by $\Delta_n = \sqrt{\Delta_{fit}^2 - \Delta_{unfld}^2 - \Delta_{det}^2}$, where $\Delta_{unfld} = 3$ ns, and $\Delta_{det} = 2.17$ ns. For the current example this gives $\Delta_n = 6.83$ ns. This results in an ion temperature measurement of $\theta = 4.21$ keV, with the same relative uncertainty described above. The two different methods for determining the ion temperature agree well with each other. For the purposes of comparison with other detectors in the facility, and with simulations, the average of the two measurements are used.

4. SUMMARY

The NIF Neutron Imaging Time-of-Flight detector system is a multi-element scintillator based detector system used for precision measurements of neutron spectra produced by highly compressed capsules of thermonuclear fuel. The NIToF system measures the direct flux form the source using a finely collimated neutron flight path

and efficient detector technologies with excellent temporal response. To quantify the scattered radiation present in the detector stream, the NIToF system includes two background measurement detectors to observe the the scattered flux produced nearby. Detailed calibration data has been collected and calculated for all detectors with the NIToF system, providing an 1%–2% uncertainty on the FWHM of the arrival time of 14.1 MeV neutrons resulting in a 3% – 6% measurement of ion temperature.

REFERENCES

1. V. W. Slivinsky, H. G. Ahlstrom, K. G. Tirsell, J. Larsen, S. Glaros, G. Zimmerman, and H. Shay, "Measurement of the ion temperature in laser-driven fusion," *Phys. Rev. Lett.* **35**, pp. 1083–1085, Oct 1975.

2. R. A. Lerche, L. W. Coleman, J. W. Houghton, D. R. Speck, and E. K. Storm, "Laser fusion ion temperatures determined by neutron time-of-flight techniques," *Applied Physics Letters* **31**(10), pp. 645–647, 1977.

3. M. D. Cable, S. P. Hatchett, and M. B. Nelson, "Neutron spectroscopy with a large neutron time-of-flight detector array (lansa) (invited)," *Review of Scientific Instruments* **63**(10), pp. 4823–4827, 1992.

4. G. Lehner and F. Pohl, "Reaktionsneutronen als hilfsmittel der plasmadiagnostik," *Zeitschrift fur Physik* **207**(1), pp. 83–104, 1967.

5. H. Brysk, "Fusion neutron energies and spectra," *Plasma Physics* **15**(7), p. 611, 1973.

6. M. D. Cable and S. P. Hatchett, "Neutron spectra from inertial confinement fusion targets for measurement of fuel areal density and charged particle stopping powers," *Journal of Applied Physics* **62**(6), pp. 2233–2236, 1987.

7. T. J. Murphy, R. A. Lerche, C. Bennett, and G. Howe, "Ion-temperature measurement of indirectly driven implosions using a geometry-compensated neutron time-of-flight detector," *Review of Scientific Instruments* **66**(1), pp. 930–932, 1995.

8. D. Wilson, W. Mead, L. Disdier, M. Houry, J.-L. Bourgade, and T. Murphy, "Scattered and (n,2n) neutrons as a measure of areal density in icf capsules," *Nuclear Instruments and Methods in Physics Research Section A: Accelerators, Spectrometers, Detectors and Associated Equipment* **488**(1–2), pp. 400 – 409, 2002.

9. V. Glebov, D. Meyerhofer, T. Sangster, C. Stoeckl, S. Roberts, C. Barrera, J. Celeste, C. Cerjan, L. Dauffy, D. Eder, R. Griffith, S. Haan, B. Hammel, S. Hatchett, N. Izumi, J. Kimbrough, J. Koch, O. Landen, R. Lerche, B. MacGowan, M. Moran, E. Ng, T. Phillips, P. Song, R. Tommasini, B. Young, S. Caldwell, G. Grim, S. Evans, J. Mack, T. Sedillo, M. Wilke, D. Wilson, C. Young, D. Casey, J. Frenje, C. Li, R. Petrasso, F. Seguin, J. Bourgade, L. Disdier, M. Houry, I. Lantuejoul, O. Landoas, G. Chandler, G. Cooper, R. Leeper, R. Olson, C. Ruiz, M. Sweeney, S. Padalino, C. Horsfield, and B. Davis, "Development of nuclear diagnostics for the national ignition facility (invited)," *Review of Scientific Instruments* **77**(10), pp. 10E715–1–7, 2006.

10. M. G. Johnson, J. A. Frenje, D. T. Casey, C. K. Li, F. H. Séguin, R. Petrasso, R. Ashabranner, R. M. Bionta, D. L. Bleuel, E. J. Bond, J. A. Caggiano, A. Carpenter, C. J. Cerjan, T. J. Clancy, T. Doeppner, M. J. Eckart, M. J. Edwards, S. Friedrich, S. H. Glenzer, S. W. Haan, E. P. Hartouni, R. Hatarik, S. P. Hatchett, O. S. Jones, G. Kyrala, S. L. Pape, R. A. Lerche, O. L. Landen, T. Ma, A. J. MacKinnon, M. A. McKernan, M. J. Moran, E. Moses, D. H. Munro, J. McNaney, H. S. Park, J. Ralph, B. Remington, J. R. Rygg, S. M. Sepke, V. Smalyuk, B. Spears, P. T. Springer, C. B. Yeamans, M. Farrell, D. Jasion, J. D. Kilkenny, A. Nikroo, R. Paguio, J. P. Knauer, V. Y. Glebov, T. C. Sangster, R. Betti, C. Stoeckl, J. Magoon, M. J. Shoup, III, G. P. Grim, J. Kline, G. L. Morgan, T. J. Murphy, R. J. Leeper, C. L. Ruiz, G. W. Cooper, and A. J. Nelson, "Neutron spectrometry—an essential tool for diagnosing implosions at the national ignition facility (invited)," *Review of Scientific Instruments* **83**(10), p. 10D308, 2012.

11. F. E. Merrill, D. Bower, R. Buckles, D. D. Clark, C. R. Danly, O. B. Drury, J. M. Dzenitis, V. E. Fatherley, D. N. Fittinghoff, R. Gallegos, G. P. Grim, N. Guler, E. N. Loomis, S. Lutz, R. M. Malone, D. D. Martinson, D. Mares, D. J. Morley, G. L. Morgan, J. A. Oertel, I. L. Tregillis, P. L. Volegov, P. B. Weiss, C. H. Wilde, and D. C. Wilson, "The neutron imaging diagnostic at nif (invited)," *Review of Scientific Instruments* **83**(10), pp. 10D317–10D317–6, 2012.

12. N. Guler, P. Volegov, C. R. Danly, G. P. Grim, F. E. Merrill, and C. H. Wilde, "Simultaneous usage of pinhole and penumbral apertures for imaging small scale neutron sources from inertial confinement fusion experiments," *Review of Scientific Instruments* **83**(10), pp. 10D316–10D316–3, 2012.

13. J. Briesmeister *et al.*, *MCNP–A general Monte Carlo code for neutron and photon transport*, Los Alamos National Laboratory, 1986.

14. J. Flournoy, "Measurement of subnanosecond scintillation decay times by time-correlated single photon counting," *International Journal of Radiation Applications and Instrumentation. Part C. Radiation Physics and Chemistry* **32**(2), pp. 265 – 268, 1988. Special Issue Milton Burton Memorial Issue.

15. J. K. Dickens, "Scinful - a monte carlo based computer program to determine a scintillator full energy response to neutron detector for en between 0.1 and 80 mev.," Technical Report ORNL-6463, Oak Ridge National Lab, Oak Ridge National Lab., TN (USA), 1988.

16. W. R. Nelson, H. Hirayama, and D. W. O. Rogers, "The egs4 code system," Technical Report SLAC-265, Stanford Linear Accelerator, 1985.

17. L. Thompson, "Neutron effects in a 2 2 nai(tl) scintillation spectrometer," *Nuclear Instruments and Methods* **25**(0), pp. 333 – 337, 1964.

18. W. Burrus and V. Verbinski, "Fast-neutron spectroscopy with thick organic scintillators," *Nuclear Instruments and Methods* **67**(2), pp. 181 – 196, 1969.

19. S. W. Haan, J. D. Lindl, D. A. Callahan, D. S. Clark, J. D. Salmonson, B. A. Hammel, L. J. Atherton, R. C. Cook, M. J. Edwards, S. Glenzer, A. V. Hamza, S. P. Hatchett, M. C. Herrmann, D. E. Hinkel, D. D. Ho, H. Huang, O. S. Jones, J. Kline, G. Kyrala, O. L. Landen, B. J. MacGowan, M. M. Marinak, D. D. Meyerhofer, J. L. Milovich, K. A. Moreno, E. I. Moses, D. H. Munro, A. Nikroo, R. E. Olson, K. Peterson, S. M. Pollaine, J. E. Ralph, H. F. Robey, B. K. Spears, P. T. Springer, L. J. Suter, C. A. Thomas, R. P. Town, R. Vesey, S. V. Weber, H. L. Wilkens, and D. C. Wilson, "Point design targets, specifications, and requirements for the 2010 ignition campaign on the national ignition facility," *Physics of Plasmas* **18**(5), p. 051001, 2011.

20. S. H. Glenzer, D. A. Callahan, A. J. Mackinnon, J. L. Kline, G. Grim, E. T. Alger, R. L. Berger, L. A. Bernstein, and et al., "Cryogenic thermonuclear fuel implosions on the national ignition facility," *Physics of Plasmas* **19**(056318), pp. 056318–1 (15 pp.), 2012.

21. A. J. Mackinnon, J. L. Kline, S. N. Dixit, S. H. Glenzer, M. J. Edwards, D. A. Callahan, N. B. Meezan, S. W. Haan, J. D. Kilkenny, and T. Doeppner, "Assembly of high-areal-density deuterium-tritium fuel from indirectly driven cryogenci implosions," *Physical Review Letters* **108**(215005), pp. 215005–1 (4 pp.), 2012.